# SUPPORTING INFORMATION

# Two-dimensional to bulk crossover of the $WSe_2$ electronic band structure

Raphaël Salazar,[†,‡] Matthieu Jamet,[¶] Céline Vergnaud,[¶] Aki Pulkkinen,[‡] François Bertran,[†] Chiara Bigi,[†] Jan Minár,[‡] Abdelkarim Ouerghi,[§] Thomas Jaouen,[‖] Julien Rault,[†] and Patrick Le Fèvre[*,†,‖]

†*Synchrotron SOLEIL, L'Orme des Merisiers, Départementale 128, F-91190 Saint-Aubin, France*

‡*New Technologies Research Centre, University of West Bohemia, 30614 Pilsen, Czech Republic*

¶*Univ. Grenoble Alpes, CEA, CNRS, Grenoble INP, IRIG-SPINTEC, 38000 Grenoble, France*

§*Université Paris-Saclay, CNRS, Centre de Nanosciences et de Nanotechnologies, 91120, Palaiseau, Paris, France*

‖*Univ Rennes, CNRS, IPR - UMR 6251, F-35000 Rennes, France*

⊥*ABB Switzerland Ltd, Baden Dättwil, Switzerland*

E-mail: patrick.lefevre@univ-rennes.fr

# ARPES measurements

The ARPES measurements were all performed at the CASSIOPEE beamline of the SOLEIL storage ring using a Scienta R4000 analyzer. The sample is installed on a vertical sample holder, with its surface normal horizontal. The photon beam is horizontal and comes at 45° from the electron analyzer axis (see Figure S1), which is mounted with its entrance slit vertical. In our measurements, we used linear horizontal (LH) polarized light. Three rotations are available to precisely align the sample with respect to the electron analyzer.

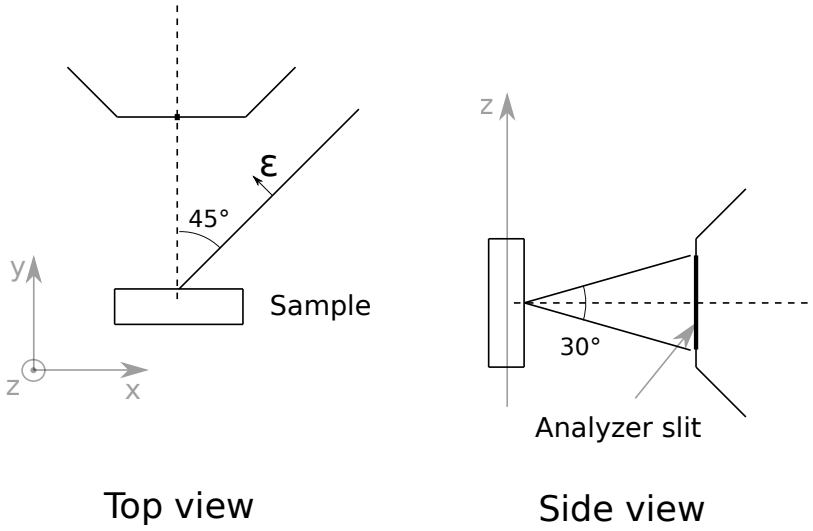


Figure S1: Top and side view of the experimental geometry showing the sample (schematized as a rectangle) and the nose of the electron analyzer. On the top view, the light is coming from the right (schematized as a solid line) at 45° from the sample normal when it is facing the analyzer. $\varepsilon$ is the polarisation vector of the beam, which was always linear horizontal in our measurements. The slit of the analyzer is vertical (along the $z$-axis, as defined at the bottom left of the figure).

- A $\theta$-rotation around the $z$-vertical axis (see bottom left of Figure S1 for the definition of the frame). This rotation is used to perform a complete 3D-band structure measurement ($k_x$,$k_y$,$E_B$) which can be cut at any electron binding energy $E_B$, giving the constant energy surfaces used below to align and characterize the samples (see Figure S2).

- A $\phi$-rotation around the sample surface normal, which can be used to align any crys-

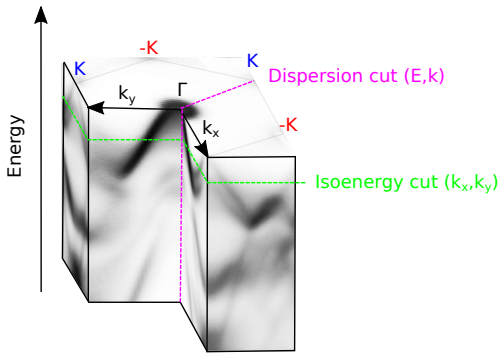


Figure S2: Example of a 3D data block ($k_x$,$k_y$,$E_B$) of the band structure of the N-layer sample.

tallographic axis of the sample along the analyzer slit.

- A Tilt-rotation around a horizontal axis contained in the sample surface plane, which was mainly used here to correct vertical angular misalignment.

For the photon energy dependant measurements presented in the main text of the paper, we used these three degrees of freedom to align the Γ-$K$ direction of the sample reciprocal space along the electron analyzer slit. Three translations along perpendicular axis are also available, first to place the sample surface at a correct measurement position, but also possibly to scan the sample surface. In this latter case, the spatial resolution is around 100 µm. All the measurement were performed at room temperature. We call $k_{\|}$ the component of the wave vector parallel to this direction. A ($k_{\|}$, $E_B$) image can then be measured at once thanks to the 2D-detector of the electron analyzer. Here, $E_B$ is the electron binding energy and is measured with respect to the Fermi level. The most efficient way to travel along $k_z$ in the reciprocal space ($\Gamma - A$ direction) is to vary the photoelectron kinetic energy $E_K$. For a photoelectron going out from the sample along the surface normal, the relation between $k_z$ and $E_K$ is given by $k_z = \sqrt{\frac{2m}{\hbar^2}(E_K + V_0)}$, where $m$ is the electron mass and $V_0$ is the so-called inner potential, a material-dependent quantity which is not known *a priori* but can be determined experimentally[1]. In bulk $WSe_2$, it was shown to be in the order of 13 eV[2] (14.5 eV in the work of Finteis *et al.*[3]). In this work, we kept the value $V_0 = 13$ eV for all

conversions. Since $E_K \simeq h\nu - E_B$, varying the photon energy corresponds to changing $k_z$. In our measurements, we used photons from 20 to 90 eV (and 1 eV-step), which amounts to span a $k_z$-range from roughly 2.5 to 5 Å$^{-1}$.

The principle of the monochromator installed on CASSIOPEE does not allow for an absolute determination of the photon energy. To calculate as precisely as possible the relative binding energies from one measurement to the other, the Fermi level energy was measured every 5 eV (at 20, 25... and 90 eV photon energies) on the Mo-clips holding the sample and connecting it to the ground. The Fermi level energy position was then extracted for each photon energy by linearly interpolating the data set, and used as the reference for the binding energies. To allow for more quantitative analysis, the intensities of the spectra were normalised to the secondary electron background intensity above the Fermi level (excited by higher harmonics of the undulator providing photons to the beamline), correcting both the detector background and the differences in flux between two photon energies.

## More details about the samples

Most of the samples were grown by Moleclar Beam Epitaxy (MBE) on graphene/SiC(0001), held at 573 K as measured by a thermocouple in contact with the sample holder) by co-evaporating W from an e-gun evaporator at a rate of 0.15 Å/min and Se from an effusion cell. The Se partial pressure measured at the sample position is fixed at $10^{-6}$ mbar. In situ Reflection High Energy Electron Diffraction (RHEED) is used to monitor the $WSe_2$ crystal structure during growth. The obtained $WSe_2$ films were then annealed at 1023 K during 15 minutes to improve the crystalline quality. Using this method, centimeter scale (here typically 1×1 cm$^2$) samples can be obtained with a precise control of their thickness, given by the amount of deposited W, Se atoms being in excess by a factor ∼20[4–6]. The graphene on SiC(0001) substrates was slightly doped[7]. Prior to their introduction in the ARPES chamber, the samples were annealed at 573 K until the pressure stabilised and

reached down P$\simeq 10^{-9}$ mbar (about three hours). The annealing aimed at eliminating most of the contamination adsorbed on the surface.

Prior to the photon energy dependence measurements, we checked the samples to assess their quality and their band structure. Because ARPES is a reciprocal space resolved technique, we can extract qualitative information about the crystallography of the sample like symmetries or surface reconstructions which will manifest in the band structure symmetry and band duplication. Chemical homogeneity can be checked as well by looking at binding energy shifts and sharpness of the bands. We review here the evidences collected by the mean of ARPES on all the samples.

## 2-layer $WSe_2$ sample

This sample was made by MBE on a graphene/SiC(0001) substrate following the procedure described above. Depending on the probed area, the band structure appears to be different. Figure S3(b) shows two dispersions along $\Gamma - K$ measured on two different locations (labelled $B_1$ and $B_2$) of the sample. There is an obvious binding energy shift in between the two band structures, of the order of 200 meV and the top band is brighter at $B_2$. A X-Y map performed by scanning the beam over a roughly $4\times4$ mm$^2$ area on the sample surface is presented on Figure S3(a). The intensity for each pixel is obtained by integrating the intensity over a binding energy range containing the top band on the $B_2$-location (coloured area in S3(b)). The sample appears to be quite homogeneous at the beam-size scale (around $50\times50$ µm$^2$), but it is clearly not true at the mm-scale.

Let's focus on the $B_1$-zone, which presents interesting characteristics. The constant energy cuts shown in Figure S4(a) a show a relatively well defined band structure with $\Gamma - K$ directions clearly visible for both graphene (denoted $\Gamma - K_{Gr}$ in the figure) and $WSe_2$ ($\Gamma - K_{WSe_2}$). The alignment $\Gamma - K_{WSe_2} - K_{Gr}$ also tells us that the $WSe_2$-layer is truly in epitaxy on graphene. The image does not have excessive azimutal smearing, meaning that the probed $WSe_2$ is essentially single domain. A second derivative of the constant

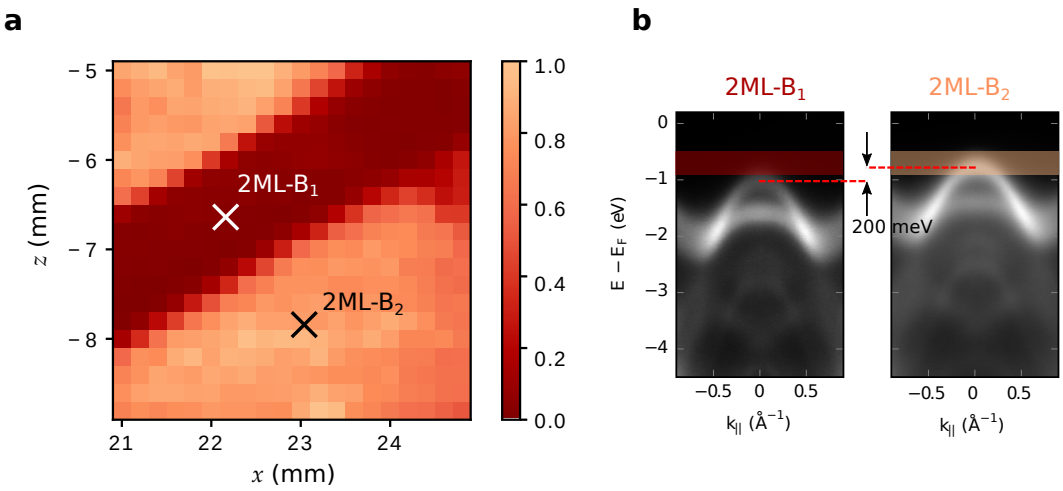


Figure S3: 2-layer sample : (a) Intensity map in the range $E_k = -1 \pm 0.2$ eV for sample 2-layer B, $h\nu = 90$ eV - LH polarization. (b) $\Gamma - K$ ARPES cuts on locations representative of the two zones, $h\nu = 60$ eV, LH polarization. The semi-transparent colored areas correspond to the parts of the signal contributing to the intensity map in (a).

energy surface highlights the double-pocket formed by the two bands at $K_{WSe_2}$ without any other contributions. However, the pocket contour loses some intensity near the $K_{Gr}$ points, certainly because of the large brightness of the latter. A zoom on a $K_{Gr}$ point for two binding energies are presented on Figure S4(b). The cut at $E_B$=-0.75 eV, near the Dirac point located at $E_D$=-0.32 eV, shows six points forming a hexagon at a distance of 0.4 Å$^{-1}$ from the center $K_{Gr}$, a signature of a graphene surface reconstruction. The cut at $E_B = -1.65$ eV, shows that the graphene $\pi$-band is actually doubled, meaning that, on the SiC-substrate, coexist single layer (SLG) and bilayer graphene (BLG). This is confirmed by the dispersion displayed in Figure S4(c). Looking in detail at Figure S3(b) we can see that the low-lying band at $\Gamma$ of the $B_1$ location is duplicated. This is because the graphene layer is not completely uniform and two thicknesses of graphene coexist at this location. The magnitude of the charge transfer being dependent on the number of graphene layers[8], the photoemission spectrum of the $WSe_2$ is duplicated. In the $B_2$-zone, there is no trace of splitting in the $\Gamma - K$ dispersion, suggesting a more uniform substrate. We used this zone for the $k_z$-measurements presented in the main text and its band structure in $\Gamma - K$ direction is shown in Figure S5.

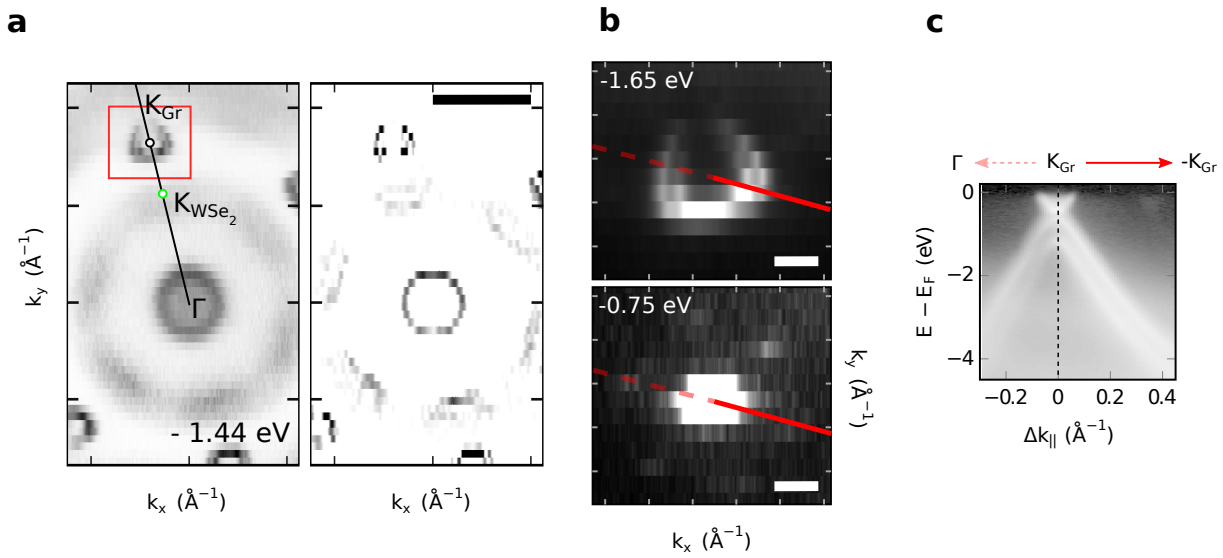


Figure S4: 2-layer sample: (a) Constant energy cut of the band structure and second derivative recorded on the $B_1$ zone. The thick black line on top indicates the scale 1 $Å^{-1}$. (b) Constant energy cuts near the graphene cone at high symmetry point $K_{Gr}$ (area surrounded by the red frame in (a)) at the two indicated binding energies. The thick white line at the bottom indicates the scale 0.2 $Å^{-1}$. (c) $\Gamma \longrightarrow K_{Gr} \longrightarrow -K_{Gr}$ ARPES cut with logarithmic color scale. The cut is made along the thick red line/dash line highlighted in (b). All measurements are done with $h\nu = 90$ with LH polarization.

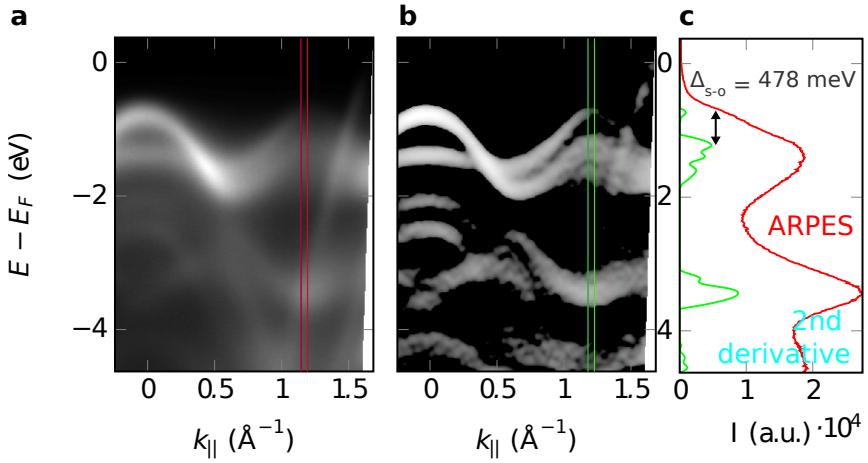


Figure S5: $\Gamma - K$ band dispersion of the 2-layer sample in $B_2$ zone. $h\nu = 60$ eV, polarization LH. (a) Raw ARPES data, (b) Second derivative, (c) EDC extracted at $K$-point from (a) in red and (b) in green.

## 3-layer $WSe_2$ sample

The 3-layer $WSe_2$ sample was grown on Mica and then wet-transferred onto a Gr-SiC substrate[4,9]. The constant energy cuts in Figure S6(a) show a well defined band structure with $K$ points with little azimutal smearing. Both the raw data and their second derivative clearly show the double pocket at $K_{WSe_2}$. Unlike for the 2-layer sample, the $K_{WSe_2}$ and $K_{Gr}$ points are not aligned but separated by an angle of 13°. It is actually not surprising since the sample was grown on a Mica substrate before being transfered onto the graphene layer. The two structures have therefore no reason to be aligned one with respect to the other. The details on the bottom of Figure S6(b) show that the graphene has the same surface reconstruction as in the 2-layer sample, although this time there is only one cone. This is visible both in the zoomed constant energy cut ($E_B$=-1.6 eV) and the ARPES cut in Figure S6(c) implying that the substrate is SLG. A dispersion $\Gamma - K$ recorded at photon energy 60 eV is presented on Figure S7. It shows the three expected bands at $\Gamma$[10].

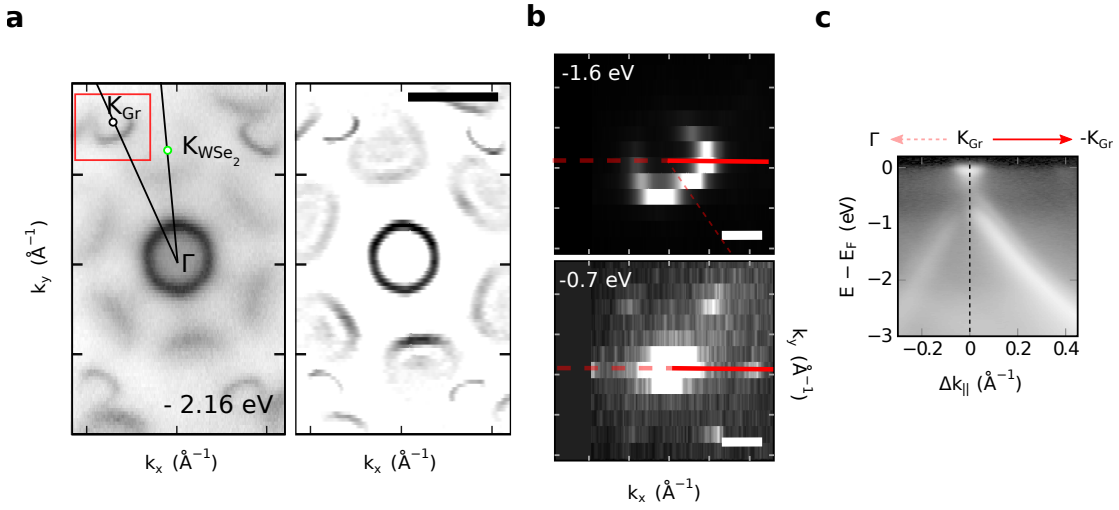


Figure S6: 3-layer sample: (a) Constant energy cut of the band structure and second derivative. The thick black line on top indicates the scale 1 $Å^{-1}$. (b) Detail of the constant energy cut near the graphene cone at high symmetry point $K_{Gr}$ at two energies. The thick white line at the bottom indicates the scale 0.2 $Å^{-1}$. (c) $\Gamma \longrightarrow K_{Gr} \longrightarrow -K_{Gr}$ ARPES cut with logarithmic color scale. The cut is made along the thick red line/dash line highlighted in b. All measurements are done with $h\nu = 90$ eV, LH polarization.

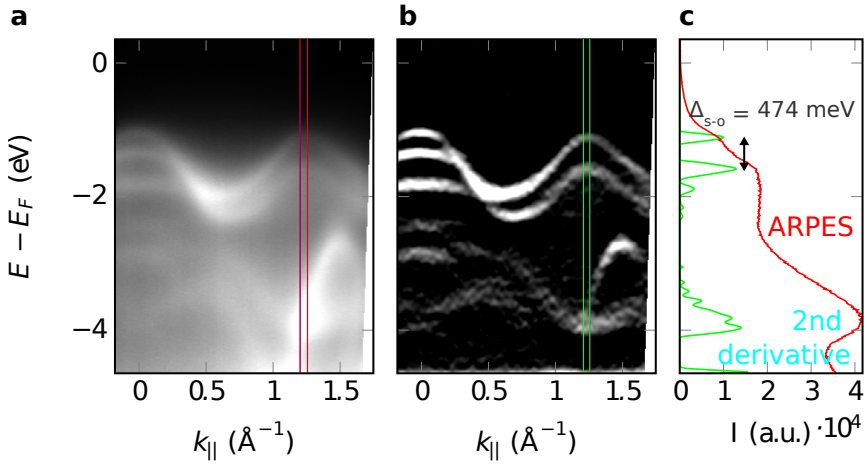


Figure S7: $\Gamma - K$ Band dispersion of the 3-layer sample. $h\nu$=60 eV, LH polarization. (a) Raw ARPES data, (b) Second derivative, (c) EDC extracted at $K$-point from (a) in red and (b) in green.

## N-layer $WSe_2$ sample

The last sample used in the work presented here is the N-layer $WSe_2$ (N-ML). The constant energy cut in Figure S8 show only the band structure of $WSe_2$ film. In this sample, the graphene is not visible anymore because of the high number of $WSe_2$ layers (thick sample). The definition of the ARPES image suggests that the sample is of very high quality with very low azimutal dispersion. Looking closely, it is possible to see ring patterns that hints at some disorder. The overall sharpness of the bands, however, is a strong indicator of the quality of the sample (see Figure S9).

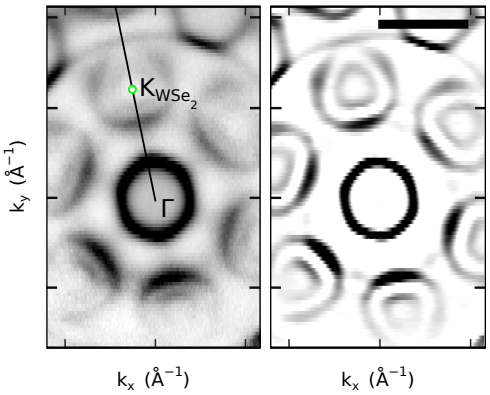


Figure S8: Sample N-ML: Constant energy cut of the band structure (left) and its second derivative (right). The thick black line on top indicates the scale 1 Å$^{-1}$.

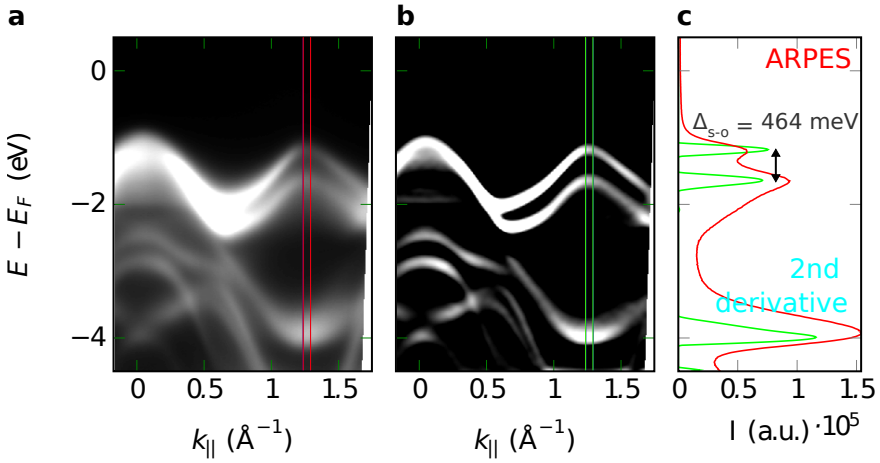


Figure S9: $\Gamma - K$ band dispersion of the N-ML sample. $h\nu$ = 60 eV, polarization LH. (a) Raw ARPES data, (b) Second derivative, (c) EDC extracted at $K$-point from (a) in red and (b) in green.

# Photon-energy dependence

Figure S10 shows the photon-energy dependent photoemission raw signal corresponding to the Figure 3 of the main text prior to the conversion to $k_z$ for the three studied samples. The top part of the figure displays the photoemission intensity integrated over a binding energy range centered on the positions of the bands. It gives a more precise view of their intensity behaviour.

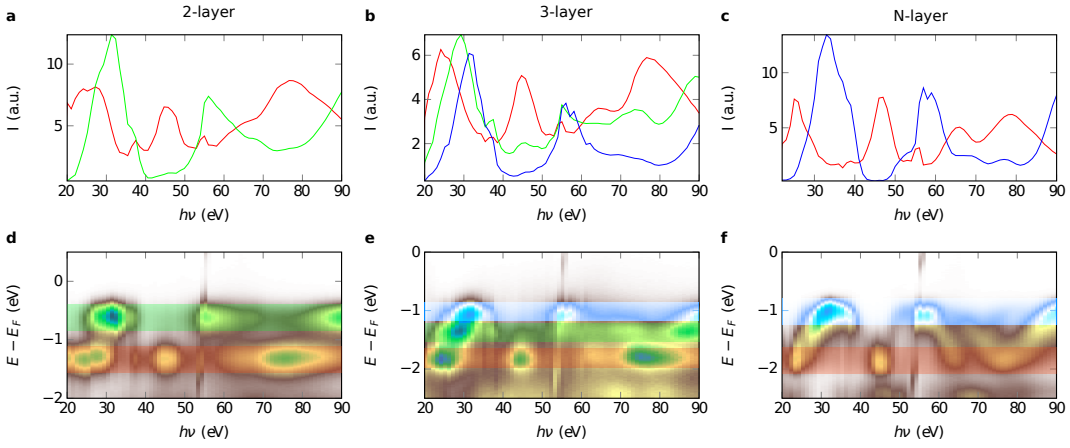


Figure S10: Bottom part: Experimental band intensity variations at $\Gamma$ along the $\Gamma - A$ direction of the reciprocal space for 2 (d), 3 (e) and N (f) layers of $WSe_2$ as a function of the photon energy. Top part: Photoemission intensity integrated over a binding energy range centered on the positions of the bands for those three samples (areas highlighted with colors on the bottom part) (a, b, c).

# Tight-binding modelisation of the $k_z$-dispersion

## Definition of the model

To model our experimental data, we developed a tight-binding model on increasingly thick $WSe_2$, retaining only the essential physics of the system and inspired by the derivations presented in references 11,12. Γ-states are principally composed of one W-5$d_{z^2}$ and two Se-4$p_z$ orbitals. To construct the tight-binding matrix, we use the states $|4p_z^{b(t)}(\mathbf{r}_{b(t),n})\rangle$ with index $b(t)$ corresponding to bottom (top) Se-atoms at position $\mathbf{r}_{b(t),n}$ inside a given layer $n$, as well as the $|5d_{z^2}(\mathbf{r}_{d,n})\rangle$ states of the W-atom located at position $\mathbf{r}_{d,n}$. The matrix describing the band structure at Γ in a single layer is given by:

$$H_1 = \begin{bmatrix} e_p & t_{pd} & 0 \\ t_{pd} & e_d & t_{pd} \\ 0 & t_{pd} & e_p \end{bmatrix} \tag{1}$$

and the interlayer Hamiltonian $H_{int}$ is given by:

$$H_{int} = \begin{bmatrix} 0 & 0 & 0 \\ 0 & 0 & 0 \\ t_{pp} & 0 & 0 \end{bmatrix} \tag{2}$$

with on-site energies $e_p$ and $e_d$ and hopping amplitudes $t_{pp} = \langle p_z^b(\mathbf{r}_{b,n+1})| H_{int} |p_z^t(\mathbf{r}_{t,n})\rangle$ and $t_{pd} = \langle d_{z^2}(\mathbf{r}_{n,d})| H_1 |p_z^{b(t)}(\mathbf{r}_{b(t),n})\rangle$. We consider that the layers are only coupled through the topmost and bottommost $p_z$ orbitals[12,13]. These amplitudes are calculated using Slater-Koster integrals $V_{pp\sigma}, V_{pp\pi}, V_{pd\sigma}, V_{pd\pi}$ which, in general, depend on the distance between the

considered atomic centers. The expression of $t_{pp}$ and $t_{pd}$ is as follows:

$$t_{pp} = (V_{pp\sigma} - V_{pp\pi}) \left(\frac{d_{XX,z}}{d_{XX}}\right)^2 + V_{pp\pi} \tag{3}$$

$$t_{pd} = V_{pd\sigma} \left( \left(\frac{d_{MX,z}}{d_{MX}}\right)^2 - \frac{1}{2}\left(\frac{d_{MX,x}}{d_{MX}}\right)^2 \right) \left(\frac{d_{MX,z}}{d_{MX}}\right) + \sqrt{3} \left(\frac{d_{MX,z}}{d_{MX}}\right) \left(\frac{d_{MX,x}}{d_{MX}}\right)^2 V_{pd\pi} \tag{4}$$

The full Hamiltonian for $N$ layers of $WSe_2$ is a $3N \times 3N$ matrix written as:

$$H_N = \begin{bmatrix} H_1 & H_{int} & & \\ H_{int}^T & H_1 & H_{int} & \\ & H_{int}^T & H_1 & \\ & & & \ddots \end{bmatrix} \tag{5}$$

We directly diagonalize $H_N$ to obtain the new eigenstates of the system, obtaining the $3N$ eigenstates $|\phi_i\rangle$ of energy $E_i$.

## Calculation of the photoemission current

The photoemission current is calculated using the Fermi-Golden rule. We assume a damped plane wave final state to mimic partial $k_z$ conservation $|\mathbf{k}_f - \frac{i}{\lambda}\mathbf{e}_\perp\rangle$. The photoemission current contributed by the state $|\phi_i\rangle = \sum_j P_{ij} |n_j, l_j, m_j, \mathbf{r}_j\rangle$ is:

$$M_{\mathbf{k}_f,\phi_i} = \langle \mathbf{k}_f + \frac{i}{\lambda}\mathbf{e}_\perp | \, \mathbf{A} \cdot \mathbf{p} \, | \phi_i \rangle \tag{6}$$

$$= -i\hbar \sum_j P_{ij} \int d^3r \mathbf{A}_0 e^{i\mathbf{k}_{h\nu}\cdot\mathbf{r}} e^{-i\left(\mathbf{k}_f + \frac{i}{\lambda}\mathbf{e}_\perp\right)\cdot\mathbf{r}} \cdot \nabla R^j_{n_j l_j}(|\mathbf{r} - \mathbf{r}_j|) Y^j_{l_j m_j}(\mathbf{r} - \mathbf{r}_j) \tag{7}$$

Being at low energy ($10 < h\nu < 100$ eV), we neglect the photon momentum $\mathbf{k}_{h\nu}$. We are only interested in the perpendicular direction to the surface i.e. $\mathbf{k}_f = k_z \mathbf{e}_\perp$ so that we only keep

the component $\mathbf{r}_i \cdot \mathbf{e}_\perp = z_i$. Following the derivation of reference 14, equation (7) becomes:

$$M_{k_z,\phi_i} \propto \left(-ik_z + \frac{1}{\lambda}\right) \mathbf{A}_0 \cdot \mathbf{e}_\perp \sum_j P_{ij} e^{-i\left(k_z + \frac{i}{\lambda}\right)\cdot z_i} \int d^3r e^{-i\left(k_z+\frac{i}{\lambda}\right)z} R^j_{n_j l_j}(r) Y^j_{l_j m_j}(\mathbf{r}) \quad (8)$$

Equation (8) involves a damped Fourier transform of the orbitals $|nlm\rangle$ that we approximate to the simple Fourier transform of $\langle \mathbf{k}|nml\rangle = f_{nl}(|\mathbf{k}|)Y_{ml}(\theta_\mathbf{k}, \phi_\mathbf{k})$[14]. In our case, this means $\langle k_z|nml\rangle = f_{nl}(k_z)Y_{ml}(0,0)$ with $f_{nl}$ such as:

$$f_{nl}(k) = 4\pi a_*^{3/2} \sqrt{\frac{(n-l-1)!}{(n+l)!}} n^2 2^{2l+2} l! \frac{(-iy)^l}{(y^2+1)^{l+2}} C^{l+1}_{n-l-1}\left(\frac{y^2-1}{y^2+1}\right) \quad (9)$$

where $a_* = a_0/Z$ ($a_0$ is the Bohr radius and $Z$ the charge of the nucleus in question) $y = nk/a_*$ and $C^{l+1}_{n-l-1}$ a Gegenbauer polynomial[11]. It follows that:

$$M_{k_z,\phi_i} \approx \sum_j P_{ij} e^{-i\left(k_z+\frac{i}{\lambda}\right)\cdot z_i} f^j_{n_j l_j}(k_z) Y^j_{l_j m_j}(0,0) \quad (10)$$

$$\approx \sum_j e^{-i\left(k_z+\frac{i}{\lambda}\right)\cdot z_i} P_{ij} M_{k_z,j} \quad (11)$$

Finally we can calculate the total photoemission current as:

$$I_{ph}(k_z, \omega) \approx \sum_i |M_{k_z,\phi_i}|^2 A(\omega - E_i) \quad (12)$$

where $A(\omega - E_i) = \frac{2\eta}{(\omega - E_i)^2 + \eta^2}$ is the broadened $E_i$ line.

## Simulation parameters

For the simulation, we used the $V_{pp\sigma} = 1.530$ eV, $V_{pp\pi} = -0.123$ eV, $V_{pd\sigma} = 5.803$ eV, $V_{pd\pi} = -1.081$ eV coefficients from reference 15. $e_p$ and $e_d = -2.7$ eV are set equal despite the different crystal fields values. This modification accounts for the missing hybridization within the layer. The distances $d_{MX,z} = 3.5881056$ Å, $d_{MX} = 1.4459472$ Å, $d_{XX,z} = 4.59299$

Å, $d_{XX} = 2.55271$ Å, are determined geometrically (see Figure S11) from the bulk crystallographic parameters[16]. In the specific case of $WSe_2$, one has to encode two contributions for the photoemission signal: one can have the sequence W-Se-Se or the sequence Se-Se-W emitting simultaneously in the $k_z$ direction. This is a simplified version of the screw axis symmetry discussed in reference 3. This corresponds to a phase factor that we include in the formula of the matrix element:

$$M_{k_z,\phi_i} \approx \sum_{\varphi \in \{0,2\pi/c\}} \sum_j e^{-i\left(k_z+\varphi+\frac{i}{\lambda}\right)\cdot z_i} P_{ij} M_{k_z,j} \tag{13}$$

This can lead to additional interferences. For the clarity of exposition, we only keep the phase term $\varphi = 2\pi/c$ which corresponds to the less-suppressed bands in the experimental data.

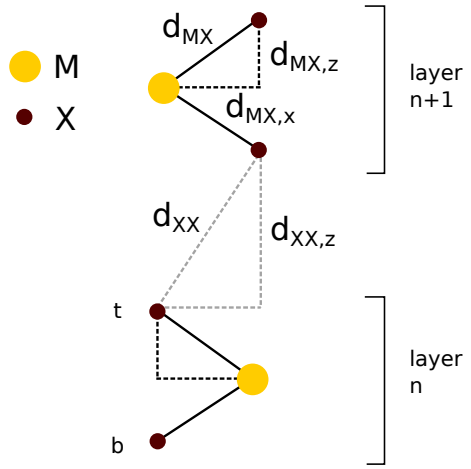


Figure S11: Geometrical model for the 1D $k_z$-dispersion of a $MX_2$ TMD.

# One-step model ARPES calculations

The structures of the 1-, 2- and 3-layer as well as bulk $WSe_2$ were constructed using the bulk lattice parameters ($a = 3.282$ Å, $c = 12.96$ Å). The electronic structure was calculated using the full potential spin-polarized relativistic Korringa-Kohn-Rostoker method (SPRKKR package)[17], which solves the Dirac equation using multiple scattering and Green's functions. The 1-, 2-, and 3-layer structures were solved within a repeated slab geometry with vacuum thickness $> 25$ Å. Exchange and correlation effects were treated at the level of local spin density approximation (LSDA) and the basis set was truncated at $l_{\max} = 3$. The ARPES calculations were performed in layer-KKR formalism with a semi-infinite surface construction. For the 1-, 2-, and 3-layer structures we set the bulk repeat sequence as vacuum, and therefore the ARPES calculation treats them as truly freestanding thin films.

# Detailed comparison of the models and experiments

## Comparison of the three simulation schemes for different 1,2,3,N-layer systems

Figure S12 summarizes the results of the different calculation strategies used in this paper for 1-, 2- and 3-layer $WSe_2$ systems as well as on a bulk crystal.

## Quantitative comparison of the eigenvalues calculated in the TB and 1-step models with experimental data

This section is dedicated to the extraction of the bands binding energies at $\Gamma$ and $K$, both in the experimental data recorded on the different samples and in simulations. This was done by fitting energy dispersion curve (EDC), i.e. vertical cuts in images like the one presented on Figure S9. To improve the signal to noise ratio, EDCs were averaged over $\pm 0.05$ Å$^{-1}$ around the points of interest. This work was done on the second derivative of experimental images

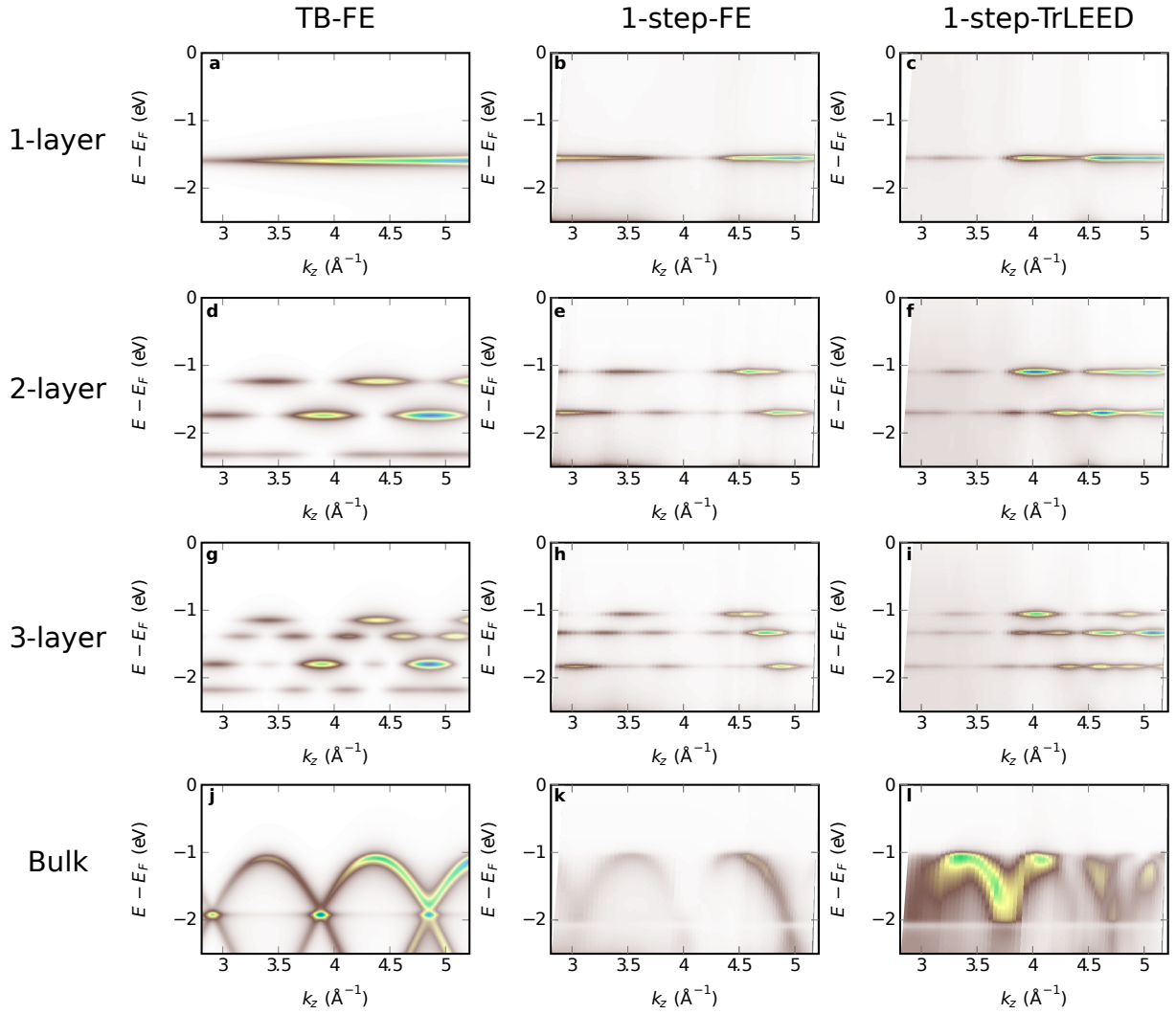


Figure S12: Comparison of $k_z$-dispersions obtained with the different models. Left: TB-FE: tight-binding initial state, free-electron final state. Middle: 1-step-FE: Bloch spectral function initial state, free-electron final state. Right: 1-step-TrLEED: Bloch spectral function initial state, time-reversed LEED final state. These calculations were performed on (from top to bottom) 1-, 2- and 3-layer $WSe_2$ systems as well as on a bulk crystal.

recorded at $h\nu = 60$ eV, a photon energy which corresponds to a bulk $\Gamma$ point (see Figure S10). For the calculations, we used the results obtained with the 1-step-TrLEED model at $h\nu = 90$ eV, another bulk $\Gamma$ point. Figure S13 shows the EDC at $\Gamma$ and $K$ extracted from the experimental data (second derivative) and the calculations. The positions of the peaks are extracted after fitting the data with appropriate line-shapes (Lorentzian for the simulations, Gaussian for the experiments). We are here only interested in the top bands of the valence

band, so lower lying bands are excluded from the fit. We calculated different quantities like $\Delta_{\Gamma-K}$, the energy difference between the top of the valence band at $\Gamma$ and at $K$, $\Delta_{s-o}$, the splitting between the two bands at $K$ and $\Delta_{\Gamma-tot}$, the total energy width containing all the bands at $\Gamma$ constituting the top of the valence band. The extracted values are summarized in table 1 and table 2. They compare well to the literature. In the case of 3-layer sample, the reported values differ slightly from the literature value in reference 9 even though the samples are identical. This might indicate a slight deviation from the $\Gamma - K$ cut in the detector or a slight evolution of the sample on a few years time span.

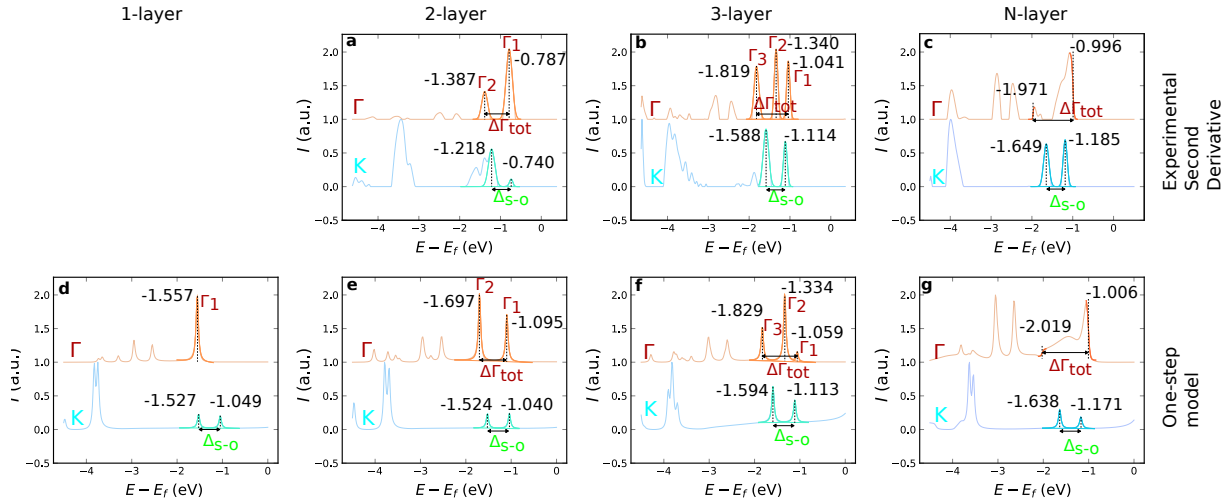


Figure S13: (a-c) Normalised experimental EDC from second derivative signal measured at $h\nu = 60$ eV for samples 2,3,N-layers (see Figures S5, S7, S9). Valence band peaks at $\Gamma$ (labeled $\Gamma_i$) and $K$ are fitted with Gaussian line-shapes. (d-g) Normalised experimental EDC from signal calculated with 1-step-TrLEED model at $h\nu = 90$ eV for samples 1,2,3,N-layers. Valence band peaks at $\Gamma$ and $K$ are fitted with Lorentzian line-shapes. For the bulk case, $\Delta_{\Gamma_{tot}}$ is obtained by locating the low binding energy side of the band using a fit with a Fermi-Dirac distributions.

Table 1: Energy differences between the three top bands of the valence band at the Γ-point ($\Delta\Gamma_{i,j}$ is the energy difference between band $i$ and band $j$; $\Delta\Gamma_{tot}$ is the energy difference between band 1 and band 3) extracted from the TB-FE calculation, the 1-step-based calculations and the experimental data (second derivative). 1-step and experimental values are calculated from the EDCs available in the Supplementary Information. We did not fit 1-step-FE data since they yield the same values as 1-step-TrLEED (same initial state). The values for the TB-FE model are calculated from the eigenvalues after diagonalization of the TB-Hamiltonian.

| | | TB | 1-step | EXP |
|---|---|---|---|---|
| 2-layer | $\Delta\Gamma_{tot}$ | 0.503 | 0.602 | 0.600 |
| 3-layer | $\Delta\Gamma_{12}$ | 0.237 | 0.275 | 0.299 |
| | $\Delta\Gamma_{23}$ | 0.410 | 0.495 | 0.479 |
| | $\Delta\Gamma_{tot}$ | 0.648 | 0.770 | 0.778 |
| N-layer | $\Delta\Gamma_{tot}$ | 0.737 | 1.013 | 0.975 |

Table 2: Energy differences (see text for the definitions) between the bands at Γ and $K$ extracted from the 1-step calculations and compared to experimental data (second derivative). Calculated from the data in Figure S13. Additional values from the literature are given in parenthesis for comparison with our results.

| | | 1-step | EXP |
|---|---|---|---|
| 1-layer | $\Delta_{\Gamma-K}$ | -0.507 | (-0.5[18]) |
| | $\Delta_{s-o}$ | 0.477 | (0.48[8]) |
| 2-layer | $\Delta_{\Gamma-K}$ | -0.055 | -0.047 (-0.080[19]) |
| | $\Delta_{s-o}$ | 0.484 | 0.478 (0.489[19]) |
| 3-layer | $\Delta_{\Gamma-K}$ | 0.054 | 0.073 (0.057[9]) |
| | $\Delta_{s-o}$ | 0.481 | 0.474 (0.480[9]) |
| N-layer | $\Delta_{\Gamma-K}$ | 0.165 | 0.189 |
| | $\Delta_{s-o}$ | 0.466 | 0.464 |

# References


(1) Hüfner, S. Photoelectron Spectroscopy: Principles and Applications, 3rd ed.; Advanced Texts in Physics; Springer-Verlag: Berlin Heidelberg, 2003.

(2) Riley, J. M. et al. Direct observation of spin-polarized bulk bands in an inversion-symmetric semiconductor. Nature Physics **2014**, 10, 835–839.

(3) Finteis, T.; Hengsberger, M.; Straub, T.; Fauth, K.; Claessen, R.; Auer, P.; Steiner, P.; Hüfner, S.; Blaha, P.; Vögt, M.; Lux-Steiner, M.; Bucher, E. Occupied and unoccupied electronic band structure of $WSe_2$. Physical Review B **1997**, 55, 10400–10411.

(4) Dau, M. T.; Vergnaud, C.; Gay, M.; Alvarez, C. J.; Marty, A.; Beigné, C.; Jalabert, D.; Jacquot, J.-F.; Renault, O.; Okuno, H.; Jamet, M. van der Waals epitaxy of Mn-doped $MoSe_2$ on mica. APL Materials **2019**, 7, 051111.

(5) Mallet, P.; Chiapello, F.; Okuno, H.; Boukari, H.; Jamet, M.; Veuillen, J.-Y. Bound Hole States Associated to Individual Vanadium Atoms Incorporated into Monolayer $WSe_2$. Phys. Rev. Lett. **2020**, 125, 036802.

(6) Dosenovic, D.; Dechamps, S.; Vergnaud, C.; Pasko, S.; Krotkus, S.; Heuken, M.; Genovese, L.; Rouviere, J.-L.; den Hertog, M.; Van-Jodin, L. L.; Jamet, M.; Marty, A.; Okuno, H. Mapping domain junctions using 4D-STEM: toward controlled properties of epitaxially grown transition metal dichalcogenide monolayers. 2D Materials **2023**, 10, 045024.

(7) Pallecchi, E.; Lafont, F.; Cavaliere, V.; Schopfer, F.; Mailly, D.; Poirier, W.; Ouerghi, A. High Electron Mobility in Epitaxial Graphene on 4H-SiC(0001) via post-growth annealing under hydrogen. Scientific Reports **2014**, 4, 4558.

(8) Zhang, Y.; Xie, X.; Zong, J.; Chen, W.; Yu, F.; Tian, Q.; Meng, Q.; Wang, C.; Zhang, Y.

Charge transfer between the epitaxial monolayer $WSe_2$ films and graphene substrates. Applied Physics Letters **2021**, 119, 111602.

(9) Salazar, R. et al. Visualizing Giant Ferroelectric Gating Effects in Large-Scale $WSe_2/BiFeO_3$ Heterostructures. Nano Lett. **2022**, 22, 9260–9267.

(10) Nguyen, P. V.; Teutsch, N. C.; Wilson, N. P.; Kahn, J.; Xia, X.; Graham, A. J.; Kandyba, V.; Giampietri, A.; Barinov, A.; Constantinescu, G. C.; Yeung, N.; Hine, N. D. M.; Xu, X.; Cobden, D. H.; Wilson, N. R. Visualizing electrostatic gating effects in two-dimensional heterostructures. Nature **2019**, 572, 220–223.

(11) Amorim, B. General theoretical description of angle-resolved photoemission spectroscopy of van der Waals structures. Physical Review B **2018**, 97, 165414.

(12) Kim, B. S.; Rhim, J.-W.; Kim, B.; Kim, C.; Park, S. R. Determination of the band parameters of bulk 2H-$MX_2$ (M=Mo, W; X=S, Se) by angle-resolved photoemission spectroscopy. Scientific Reports **2016**, 6, 36389.

(13) Cappelluti, E.; Roldán, R.; Silva-Guillén, J. A.; Ordejón, P.; Guinea, F. Tight-binding model and direct-gap/indirect-gap transition in single-layer and multilayer $MoS_2$. Physical Review B **2013**, 88, 075409.

(14) Moser, S. An experimentalist's guide to the matrix element in angle resolved photoemission. Journal of Electron Spectroscopy and Related Phenomena **2017**, 214, 29–52.

(15) Silva-Guillen, J. A.; San-Jose, P.; Roldan, R. Electronic Band Structure of Transition Metal Dichalcogenides from Ab Initio and Slater–Koster Tight-Binding Model. Applied Sciences **2016**, 6, 284.

(16) Schutte, W.; De Boer, J.; Jellinek, F. Crystal structures of tungsten disulfide and diselenide. Journal of Solid State Chemistry **1987**, 70, 207–209.

(17) Ebert, H.; Ködderitzsch, D.; Minár, J. Calculating condensed matter properties using the KKR-Green's function method—recent developments and applications. Reports on Progress in Physics **2011**, 74, 096501.

(18) Mo, S.-K.; Hwang, C.; Zhang, Y.; Fanciulli, M.; Muff, S.; Dil, J. H.; Shen, Z.-X.; Hussain, Z. Spin-resolved photoemission study of epitaxially grown $MoSe_2$ and $WSe_2$ thin films. Journal of Physics: Condensed Matter **2016**, 28, 454001.

(19) Zhang, Y. et al. Electronic Structure, Surface Doping, and Optical Response in Epitaxial WSe2 Thin Films. Nano Letters **2016**, 16, 2485–2491.